CHEMISTRY OF MATERIALS
Cite This: Chem. Mater. 2018, 30, 4543−4555
Article
pubs.acs.org/cm

Understanding the Effects of Cd and Ag Doping in Cu_2ZnSnS_4 Solar Cells

Gopalakrishnan Sai Gautam,[†] Thomas P. Senftle,[†,§] and Emily A. Carter*[,‡]

[†]Department of Mechanical and Aerospace Engineering and [‡]School of Engineering and Applied Science, Princeton University, Princeton, New Jersey 08544-5263, United States

Supporting Information

ABSTRACT: Cu_2ZnSnS_4-based solar cells, which constitute an inexpensive, beyond-Si photovoltaic technology, often suffer from low open-circuit voltage and efficiency. This drawback is often attributed to disorder in the Cu−Zn sublattice of the kesterite structure. While previous experiments have reported improved performances with isovalent substitution of Cd and Ag for Cu and Zn, respectively, the fundamental driving force for such improvements remains unclear. Here, we use density functional theory to study bulk stability, defect, and surface energetics, as well as the electronic structure of these dopants in Cu_2ZnSnS_4. We find that Cd and Ag can increase efficiencies, depending on the dopant concentration and Cu content used during synthesis. Most importantly, we find that a low level of Cd doping can suppress disorder in the kesterite phase across all Cu concentrations, while a low level of Ag doping can do so only when Zn- and Sn-rich conditions are employed. A higher Ag content is beneficial as it stabilizes the kesterite structure, whereas a higher Cd content is detrimental as it stabilizes the lower-gap stannite structure. Cd does not significantly influence the surface energetics of kesterite Cu_2ZnSnS_4. Ag, on the other hand, decreases the surface energies significantly, which would favor smaller particle sizes. We thus attribute the coarsening of particle size and changes in morphology observed during Cu_2ZnSnS_4 synthesis to annealing conditions during sulfurization and selenization, instead of any effect of Cd or Ag. Finally, we suggest the exploration of abundant, nontoxic, isovalent dopants, i.e., different from the attributes of Cd and Ag, to improve the performance of Cu_2ZnSnS_4.

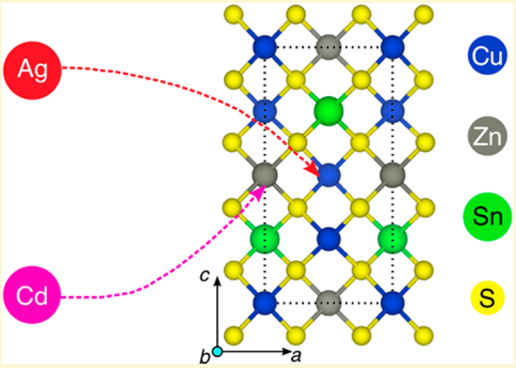

INTRODUCTION

Photovoltaic (PV) technology, which converts solar irradiation directly into usable electricity, is an important source of clean and sustainable electricity. Commercially, multicrystalline silicon (Si) PVs, with efficiencies of ∼20%,[1,2] constitute the state of the art, because of the abundance of Si and highly optimized fabrication methods. However, Si PVs suffer from poor light absorption arising from the indirect band gap of crystalline Si and consequently require thick Si layers that then increase the cost, amount of material used, and energy of production.[3] Thin-film, beyond-Si technologies,[4] which rely on direct band gap semiconductors such as GaAs,[5] CdTe,[6] $Cu(In,Ga)(S,Se)_2$,[7] and organic−inorganic hybrid perovskites,[8] have been developed to overcome the limitation imposed by the intrinsic properties of Si. However, these compound semiconductor materials are made of rare (such as Ga) or toxic elements (such as Cd, Pb, or As), which inhibits their potential as commercial PV technologies.[9] Developers of beyond-Si solar cells therefore are still searching for materials that have high efficiency and are cheap, abundant, and nontoxic.

Among various beyond-Si candidates, Cu_2ZnSnS_4-based cells display promise because the light-absorbing component is comprised of abundant, environmentally friendly elements, is cheap to process, and has an ideal single-junction band gap (1.4−1.6 eV).[10,11] Typically, Cu_2ZnSnS_4 is selenized, i.e., Se is introduced into the S sublattice, allowing the band gap of Cu_2ZnSnS_4 to be tuned[12] to improve the power conversion efficiency.[13,14] Despite its ideal band gap, Cu_2ZnSnS_4 suffers from poor efficiencies (a maximum of ∼12.6% in Se-doped cells[15]) that are significantly lower than the ≥20% observed in $Cu(In,Ga)(S,Se)_2$-, CdTe-, and Si-based cells.[2] Poor efficiency caused by band-gap narrowing has been attributed to the near-degeneracy of the kesterite and stannite polymorphs, which leads to disorder in the Cu and Zn sublattices (i.e., formation of Cu_{Zn} and Zn_{Cu} antisite defects, respectively).[16−22] Previous work has shown that Cu vacancies (Vac_{Cu}), which are more likely to form under Zn-rich conditions, can improve efficiencies.[23,24] Thus, Cu_2ZnSnS_4 is ideally synthesized under both Cu-poor and Zn-rich conditions to achieve high efficiency.[20,24−26]

One strategy for reducing disorder on the Cu−Zn sublattice (and thereby improving efficiency) is to use isovalent dopants that destabilize Cu_{Zn} and Zn_{Cu} antisite defects.[27,28] In general,

Received: February 13, 2018
Revised: June 16, 2018
Published: June 18, 2018

DOI: 10.1021/acs.chemmater.8b00677
Chem. Mater. 2018, 30, 4543−4555

antisite defect formation is facilitated if the cations forming the antisites have similar ionic radii,[21] such as ~0.6 Å for both Cu^+ and Zn^{2+} in tetrahedral coordination.[29] Thus, ions that are isovalent with Cu^+ or Zn^{2+} with ionic radii significantly different compared to those of Cu^+ or Zn^{2+} are doping candidates that can potentially inhibit the formation of antisites. For example, Cd^{2+} (with an ionic radius of 0.78 Å vs an ionic radius of 0.6 Å for Zn^{2+}) and Ag^+ (1 Å vs 0.6 Å for Cu^+) are promising candidates.[29] Indeed, experiments have demonstrated a significant improvement in efficiencies of Cu_2ZnSnS_4 cells that are doped with either Cd^{2+} or Ag^+.[30−33]

Interestingly, both Cd^{2+} and Ag^+ exhibit a peak in the open-circuit voltage (V_{oc}) and efficiency as a function of doping content.[30,31] For example, Cd^{2+}-doped cells achieve a peak V_{oc} and an efficiency of ~0.438 V and 8%, respectively, at 5% Cd doping in selenized Cu_2ZnSnS_4 cells.[30] Analogously, a peak efficiency of ~11% at 40% Cd doping has been reported in $Cu_2Zn_xCd_{1-x}SnS_4$ cells.[34] Similarly, Ag^+-doped cells exhibit a maximum V_{oc} of ~0.422 V and a peak efficiency of ~9.8% at 3−5% Ag doping.[31] Note that 5% Ag doping refers to a substitution of 5% for all Cu sites with Ag, which corresponds to a Ag concentration (x_{Ag}) of 0.025 per S. Similarly, 5% Cd doping reflects a Cd concentration (x_{Cd}) of ~0.0125 per S. Also, both Cd^{2+} doping and Ag^+ doping cause an increase in the particle size of the synthesized Cu_2ZnSnS_4 during the high-temperature selenization process.[30,31] It therefore is unclear whether Cd and Ag doping improves performance via destabilizing antisites in the bulk or via stabilizing certain surface facets and enhancing grain growth, which could decrease the number of charge-carrier trap sites at grain boundaries.

In this work, we evaluate the formation energy of various neutral and charged antisite defects in pure Cu_2ZnSnS_4, at dilute Cd and Ag doping levels (x_{Cd} and x_{Ag} ~0.015 per S), and at high concentrations of Ag and Cd (x_{Cd} ~ 0.125 per S, and x_{Ag} ~ 0.25 per S) using a variety of density functional theory (DFT)[35,36]-based calculations. We consider the formation of neutral antisites under three distinct chemical conditions, namely, Cu-rich (presence of ZnS, SnS, and Cu metal during synthesis), constrained Cu-poor (presence of ZnS, SnS, and Cu-deficient phases), and Cu-poor (S-rich and Zn-, Sn-, and Cu-deficient phases). To estimate the impact of antisites on the hole conductivity of Cu_2ZnSnS_4, we calculate the formation energies and the (charge) transition energy levels of a few lowest-energy ionized antisite defects. In addition, we assess the stability of the kesterite and stannite polymorphs as a function of Ag and Cd concentrations and the influence of Ag and Cd doping on the respective energies of (110) and (112) surface facets in kesterite (i.e., the most stable, and therefore most relevant, facets of this material). Our results indicate that Cd doping and Ag doping exhibit qualitatively different behaviors with doping. For example, under dilute doping conditions, Cd inhibits the formation of antisites under all Cu conditions, whereas Ag suppresses antisite formation only under Cu-rich conditions. Similarly, Cd and Ag stabilize the stannite and kesterite polymorphs, respectively, at high levels of doping. Additionally, at low doping concentrations and under Cu-poor conditions, Cd (Ag) is not (is) expected to significantly enhance hole conductivity within the kesterite structure. Our calculations also indicate that, while Cd doping has a negligible impact on the surface energies of kesterite, Ag doping can significantly decrease the energies of (110) and (112) surfaces. Thus, the significant particle coarsening observed during Cu_2ZnSnS_4 synthesis experimentally is not caused by either Cd or Ag doping but rather may be attributed to selenization conditions. Our results indicate that a careful tuning of both the chemical conditions during synthesis and the extent of doping are required to maximize performance. Previous theoretical studies[20,27,28,37−39] have calculated the antisite formation energies, but they have done so only at dilute Cd and Ag doping levels, signifying the depth and importance of our current study.

METHODS

We calculated the bulk, defect, and surface energetics of Cu_2ZnSnS_4 in this work using spin-polarized DFT, as implemented in the Vienna ab initio simulation package (VASP),[40,41] and employing the projector-augmented-wave (PAW)[42] theory. We use a kinetic energy cutoff of 520 eV for the plane wave basis. The orbitals are sampled on a well-converged k-point mesh (energy converged within <0.05 meV/atom) with a density of at least 1728 k-points per reciprocal atom (where k_i is the number of k-points in the ith direction).[43] We began by using the strongly constrained and appropriately normed (SCAN)[44,45] functional for describing the electronic exchange-correlation (XC) for all bulk and defect calculations, because SCAN satisfies all 17 known constraints for the behavior of an XC functional, unlike the generalized gradient approximation (GGA).[46] We also benchmarked the SCAN-predicted formation enthalpies of binary Cu, Zn, Sn, Cd, and Ag sulfides (Figure S1) and the lattice parameters of layered SnS_2 and kesterite Cu_2ZnSnS_4 (Table S1) against experimental values and found fair agreement between SCAN-predicted and experimental quantities.

Notably, our benchmarking indicates that SCAN does not predict band gaps of semiconductors accurately, with calculated eigenvalue gaps of ~0.13 and ~0.05 eV for kesterite and stannite Cu_2ZnSnS_4, respectively (Figure S2e,f). These values are significantly lower than those reported experimentally (~1.4−1.6 eV[47,48]) and theoretical values employing advanced many-body methods (1.33−1.64 eV[49]). Indeed, the performance of SCAN is of similar quality to that of GGA, which is well-known for underestimating band gaps of semiconductors[50] for the case of kesterite and stannite Cu_2ZnSnS_4 (Figure S2c,d). Therefore, we used GGA+U+D calculations[51,52] to perform qualitative comparisons of band gaps in the kesterite and stannite structures with Cd and Ag doping (Figure S3). We use U values derived from embedded Hartree−Fock calculations, namely, 3.6 eV for Cu, 4.5 eV for Zn, and 4.8 eV for Sn.[53] In the case of Ag and Cd doping, we used the U values derived for Cu and Zn, respectively, to be consistent in describing the electronic structure of Cu/Ag and Zn/Cd pairs. For relaxing the bulk structure within the GGA+U framework, we also added dispersion corrections using the D2 method of Grimme (resulting in GGA+U+D),[52] in accordance with previous work.[21] Note that these dispersion corrections are applied *a posteriori* and therefore affect only forces and hence the relaxation of a structure.

Bulk Structure. Figure 1 displays the structure of the kesterite (panel a) and stannite (panel b) polymorphs of Cu_2ZnSnS_4.[21,54] Cu, Zn, Sn, and S atoms are indicated by blue, gray, green, and yellow circles, respectively. The dashed black line indicates the extent of the conventional unit cell. Cations (Cu, Zn, and Sn) and anions (S) are both in a tetrahedral coordination environment in both structures. The main difference between kesterite and stannite arises from the stacking of the cations along the c-direction. While distinct Sn+Cu (indicated by the legend "Sn-plane" in Figure 1a) and Zn+Cu ("Zn-plane") planes form in the kesterite, segregation of Cu atoms in stannite leads to the formation of exclusive Cu (indicated by "Cu-plane" in Figure 1b) and Sn+Zn ("Zn/Sn-plane") planes. Notably, a previous study predicted near-degeneracy for the two structures with the Cu_2ZnSnS_4 composition.[21] Within the kesterite structure (Figure 1a), each Zn (Sn) atom has six Cu and two Sn (Zn) atoms that are the nearest cations, at a distance of ~3.84 Å. Four of the nearest Cu

DOI: 10.1021/acs.chemmater.8b00677
Chem. Mater. 2018, 30, 4543−4555

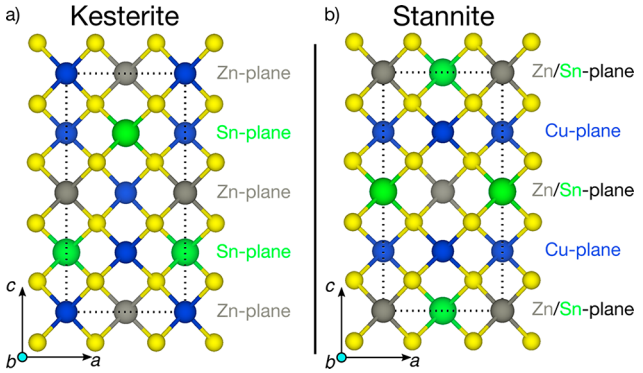

Figure 1. Structures of the (a) kesterite and (b) stannite polymorphs of Cu_2ZnSnS_4.[21,54] The dashed black lines indicate the conventional unit cells of the corresponding structures. Blue, green, gray, and yellow circles correspond to Cu, Sn, Zn, and S, respectively.

atoms are located in the same Zn (Sn) plane for each Zn (Sn) atom, while two Cu and two Sn (Zn) atoms are placed in an adjacent Sn (Zn) plane along the *c*-direction.

Surface Energies. We calculate surface energies in pure, Cd-doped, and Ag-doped Cu_2ZnSnS_4 by using GGA+*U*+*D* instead of SCAN to directly compare with previous calculations that used GGA +*U*+*D* to estimate cleavage energies in the Cu_2ZnSnS_4 system.[21] We ensured minimum slab and vacuum thicknesses of 11 and 15 Å, respectively, in all of our surface calculations, based on previously reported convergence tests.[21,55−59] Note that we use pseudo-hydrogens[59,60] to cap one of the terminating surfaces while calculating the (112) and (110) surface energies of the kesterite structure. On (112) and (110) terminations containing dangling bonds around a S atom, we used pseudo-hydrogens with fractional core (and electronic) charges of +0.25, +0.5, and +1 to mimic S−Cu (or S−Ag), S−Zn (or S−Cd), and S−Sn bonds, respectively. Similarly, on cation-terminated (112) and (110) terminations with dangling S bonds around a cation, we used a +1.5 fractional-core-charged pseudo-hydrogen to replicate a S atom. Typically, fractional charges of pseudo-hydrogens are determined by the coordination environment of a given atom based on electron counting rules.[61,62] For example, each Cu atom is coordinated by four S atoms in a tetrahedral environment within kesterite (Figure 1a), corresponding to four Cu−S bonds. Given that each Cu atom contributes one valence electron, the electronic contribution from Cu in each of the four Cu−S bonds is 0.25. Therefore, when a S atom on the surface has a dangling bond that is missing a Cu atom, a pseudo-hydrogen with a core charge of 0.25 is introduced to saturate the bond. Although the pseudo-hydrogen approach does not prevent the calculation of "relative" surface energies, i.e., $E_{\text{surface}}^{\text{doped}} - E_{\text{surface}}^{\text{pristine}}$, calculating absolute surface energies requires complex geometries to decouple the energetic contributions from the pseudo-hydrogens.[63] The surface energy with pseudo-hydrogens is defined as $E_{\text{surface}} = (E_{\text{slab+pseudo-H}} - nE_{\text{bulk}})/(2A)$, where $E_{\text{slab+pseudo-H}}$, n, E_{bulk}, and A correspond to the energy of the slab model with pseudo-hydrogens, the number of conventional unit cells used to construct the slab model, the energy of a pristine conventional cell without pseudo-hydrogens, and the area of the surface, respectively. Positions of pseudo-hydrogens were determined on the basis of the bond distances in pseudomolecules, which resemble the coordination environment for a given ion. For example, we use the relaxed ionic positions from a tetrahedral CuH_4 pseudomolecule (core charge of H = +1.5), which resembles the tetrahedral coordination of Cu by four S atoms within kesterite, to determine the location of a pseudo-hydrogen that represents a S atom in a dangling Cu−S bond (Figure 1a). Calculations of pseudomolecules are done using the GGA+*U*+*D* functional (and the same approximations as mentioned above). Calculations with capped hydrogens included a minimum of three frozen atomic layers (forces of <0.05 eV/Å) to mimic the semi-infinite bulk structure below the surface.

Defect Formation Energies. The formation energy of any defect within a pristine crystal structure is given by[50]

$$E_{\text{defect}}^{\text{formation}} = E_{\text{defect}}^{\text{supercell}} - E_{\text{bulk}}^{\text{supercell}} - \sum_i n_i\mu_i + qE_{\text{F}} + E_{\text{corr}}$$

where $E_{\text{defect}}^{\text{supercell}}$ ($E_{\text{bulk}}^{\text{supercell}}$) corresponds to the DFT-SCAN-calculated energy of a supercell with (without) the defect, n_i is the number of atoms of species i added (>0) or removed (<0) to create the defect, μ_i is the corresponding chemical potential, and E_{F} and E_{corr} are the Fermi energy of the pristine bulk structure and electrostatic correction terms, respectively, which are relevant only for charged defect calculations (with charge q).[64] We employ SCAN to calculate the formation energies of neutral defects, i.e., all valence electrons are added (removed) for each atomic species that is added (removed), while employing GGA+*U*+*D* for calculating formation energies of charged defects, i.e., donor or acceptor defects with ionized electrons or holes (see below). A 2 × 2 × 2 supercell of the conventional kesterite structure, corresponding to 64 S atoms, is used for all defect calculations. Notably, the Cu−S (2.29 Å) and Zn−S (2.33 Å) bond distances "far" from the defect within a 2 × 2 × 2 supercell are identical to the DFT-SCAN-relaxed Cu−S and Zn−S bond distances within the pristine kesterite structure, justifying the supercell size used for neutral defect calculations. The chemical potentials employed in this work (μ_i) are referenced to the SCAN energies of the pure elements in their ground-state structures at 0 K, i.e., $\mu_i^0 = \mu_i(\text{SCAN, 0 K}) \equiv 0$. To calculate the 0 K SCAN energies of pure elements, we use face-centered cubic Cu and Ag, hexagonal-close-packed Cd and Zn, cubic-diamond α-Sn, and orthorhombic α-S. All initial structures used in this work are obtained from the inorganic crystal structure database (ICSD)[54] and subsequently relaxed within DFT-SCAN.

In the case of charged defect calculations (i.e., $q \neq 0$) in periodic solids, the spurious electrostatic interactions of the charged defect with its periodic images and the homogeneous background charge used to render the cell electrostatically neutral to avoid divergences are typically corrected by evaluating the E_{corr} term.[50] One method of estimating E_{corr} is to separate the spurious electrostatic interactions into a long-range [$\sim 1/(\varepsilon r)$, dominated by interactions beyond supercell boundaries and screened by the dielectric constant, ε] and a short-range (interactions within the supercell) component, as initially developed by Freysoldt et al.[64] Typically, the long-range component is evaluated by assigning a point charge (PC)[65] or a Gaussian charge distribution[66] to the defect and its periodic images. On the other hand, the short-range term is considered to be the difference between the DFT-evaluated electrostatic potential between the defective and pristine supercells, where an "alignment" term is chosen such that short-range electrostatic interactions decay to zero far from the defect.[50] Thus, $E_{\text{corr}} = E_{\text{PC}} - q\Delta V$, where E_{PC} is the electrostatic energy from long-range interactions and ΔV is the alignment term.

Note that the formation energy of charged defects in semiconductors depends strongly on the Fermi level (E_{F}, set to 0 at the valence band maximum) within the band gap, necessitating usage of an appropriate XC functional that yields at least a qualitatively correct gap. Given that SCAN grossly underestimates the band gap of kesterite Cu_2ZnSnS_4 (Figure S2), we chose the GGA+*U*+*D* functional for all charged defect calculations considered in this work. Notably, formation energies of neutral defects, which are independent of E_{F}, computed with GGA+*U*+*D* are in fair agreement with SCAN values [with the exception of Ag on Zn antisites (see Table S8)]. Importantly, we evaluate charged defect energetics only under low Cd or Ag doping levels and use the same initial configurations as those of the lowest-formation energy configurations in SCAN. Because the tetragonal kesterite structure (Figure 1a) is anisotropic, we employ the extension of the Freysoldt correction scheme[64,66] to anisotropic systems by Kumagai and Oba (see Figures S4 and S5),[65] as implemented in the python charged defect toolkit (PyCDT).[67] The convergence of the short-range electrostatic potential to a constant value far from the defect within the Freysoldt correction scheme (Figure S4) justifies the use of a 2 × 2 × 2 supercell for our charged defect calculations. Moreover, we plot the variation in the charged defect formation energy for the Ag_{Cu} antisite (q = 1) as a function of

DOI: 10.1021/acs.chemmater.8b00677
Chem. Mater. 2018, 30, 4543−4555

the supercell size used (up to 3 × 3 × 3) in Figure S6 to demonstrate fair convergence (~0.1 eV) employing a 2 × 2 × 2 supercell. The values of E_{corr} for all charged defects considered are provided in Table S7, while the dielectric tensor, calculated using density functional perturbation theory (as implemented in VASP), is listed in Table 1.

Table 1. Dielectric Tensor of Pristine Kesterite Cu_2ZnSnS_4, Calculated Using GGA+*U*+*D*[a]

contribution	ε_{xx}	ε_{yy}	ε_{zz}
electronic	7.85	7.85	7.87
ionic	1.84	1.84	2.26
net	9.69	9.69	10.13

[a]The "net contribution" reflects the summation of the electronic and ionic contributions, which in turn is used in estimating E_{corr} in charged defect calculations (Table S7). The off-diagonal components of the dielectric tensor (ε_{ij}) are ~0.

Phase Diagrams and Chemical Potentials. Quinary phase diagrams, namely, for Cu−Zn−Sn−S−Cd and Cu−Zn−Sn−S−Ag systems, at 0 K are built using the DFT-SCAN-calculated energies. All binary, ternary, quaternary, and quinary compounds in the aforementioned chemical space, whose structures are available in the ICSD,[54] are simulated using SCAN. Note that we consider only structures that are ordered, i.e., structures in which all available sites are occupied by one element only. A list of all compounds used and their corresponding space groups are provided in Table S2. The python materials genomics (pymatgen) library was used for constructing the phase diagrams.[68] In general, a thermodynamic "facet" indicates the set of compounds (or phases) that can exist in equilibrium. Thus, the chemical potentials of all species are uniquely defined in a given facet. The facets that contain the kesterite Cu_2ZnSnS_4 structure, i.e., conditions under which kesterite Cu_2ZnSnS_4 can exist at equilibrium, and the corresponding chemical potentials are listed in Tables S3 (pure Cu_2ZnSnS_4), S4 (for Cd substitution), and S5 (for Ag substitution).

We consider three scenarios while evaluating the constraints on chemical potentials used in calculating neutral defect formation energies. (i) Cu-rich: Cu_2ZnSnS_4 is in equilibrium with metallic Cu. As Zn-rich and Sn-rich conditions during Cu_2ZnSnS_4 are preferred during synthesis,[26] we constrain the Zn and Sn chemical potentials to be in equilibrium with ZnS (Zn-rich phase) and SnS (Sn-rich), respectively. (ii) Constrained Cu-poor: the lowest (most negative) Cu chemical potential that Cu_2ZnSnS_4 can attain while ensuring equilibrium with both ZnS (Zn-rich) and SnS (Sn-rich). The Zn and Sn chemical potentials therefore are constrained in this scenario. (iii) Cu-poor: the most negative Cu chemical potential of Cu_2ZnSnS_4 without any constraints being placed on the chemical potentials of the other species (Zn, Sn, S, and Cd/Ag). In the case of Cd and Ag doping, we consider the Cd- and Ag-containing phases exhibiting the highest (least negative) possible Cd and Ag chemical potentials, respectively, while in equilibrium with Cu_2ZnSnS_4 for each of the aforementioned conditions. The explicit equations for all three conditions (including equilibrium criteria under Cd and Ag doping) considered are provided in Table S6. Note that we employ the GGA +*U*+*D* functional to compute the energetics of charged defects in Cu_2ZnSnS_4. However, GGA+*U* is not an appropriate functional for calculating the energy of a pure metal with a highly delocalized electronic structure, such as pure Cu. Hence, we calculate the charged defect formation energies only under Cu-poor conditions, because there are no metallic phases that are in equilibrium with Cu_2ZnSnS_4 (Tables S4−S6). To generate the chemical potentials of all species under Cu-poor conditions in charged defect calculations, we compute the energies of all relevant binary, ternary, and quaternary compounds with GGA+*U*+*D*.

RESULTS

Pure Cu_2ZnSnS_4. Figure 2 plots the formation energies of various neutral defects against the Cu chemical potential in undoped kesterite Cu_2ZnSnS_4. The formation energy of a defect in a given structure is indicative of the energy penalty for the defect to form within the structure. Thus, a formation energy of less than zero indicates the spontaneous formation of a defect within pristine kesterite Cu_2ZnSnS_4 (Figure 2), at a low concentration of dopants. Negative formation energies at high doping concentrations typically lead to the formation of secondary phases via side reactions that eventually destabilize the host material. The notation used to indicate each defect in Figure 2 (and the rest of the manuscript) is that of X_y, where X is a defect species on a y site. For example, Vac_{Cu} indicates a vacancy on a Cu site. Note that all vacancy defects considered are indicated by dashed lines in Figure 2. The green and orange lines, with the corresponding notation of "(Sn)" and "(Zn)", indicate a defect occurring on the Sn and Zn planes, respectively. For example, "Vac_{Cu} (Sn)" indicates a Cu vacancy on a Sn plane in the kesterite structure. Similarly, Vac_{Zn} (dashed black line in Figure 2), by definition, occurs on a Zn plane.

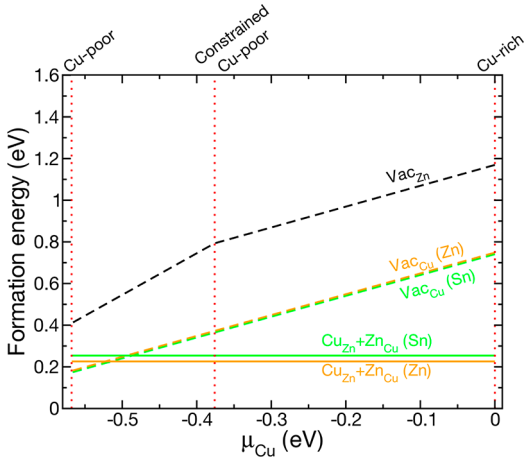

Figure 2. Formation energies, based on DFT-SCAN, of various defects in pure kesterite Cu_2ZnSnS_4 plotted vs the chemical potential of Cu. The notations "(Sn)" and "(Zn)" indicate a defect occurring on the Sn and Zn planes of the kesterite structure (Figure 1), respectively. Vac indicates vacancy.

Disorder in the Cu and Zn sublattices of the kesterite structure is modeled using a combination of two antisite defects, namely, Cu_{Zn} and Zn_{Cu} (solid lines in Figure 2), which occur on neighboring Cu and Zn sites. Thus, a combination of Cu_{Zn} and Zn_{Cu} antisites indicates an exchange of Cu and Zn atoms within the kesterite structure, representing disorder in the Cu and Zn sublattices. Additionally, for Cu_{Zn}+Zn_{Cu} combination defects, "(Sn)" and "(Zn)" indicate the plane of the Cu site that is replaced by the Zn atom. For example, "Cu_{Zn}+Zn_{Cu} (Sn)" (solid green line in Figure 2) indicates an exchange of a Zn atom with a neighboring Cu atom in an adjacent Sn plane. Similarly, "Cu_{Zn}+Zn_{Cu} (Zn)" (solid orange line in Figure 2) indicates an exchange of neighboring Zn and Cu atoms on the same Zn plane.

Kesterite Cu_2ZnSnS_4 is stable with respect to other compounds within the Cu−Zn−Sn−S quaternary phase diagram for a narrow range of Cu chemical potentials [from μ_{Cu} = 0 eV in Cu-rich to μ_{Cu} = −0.57 eV in Cu-poor (dashed

DOI: 10.1021/acs.chemmater.8b00677
Chem. Mater. 2018, 30, 4543−4555

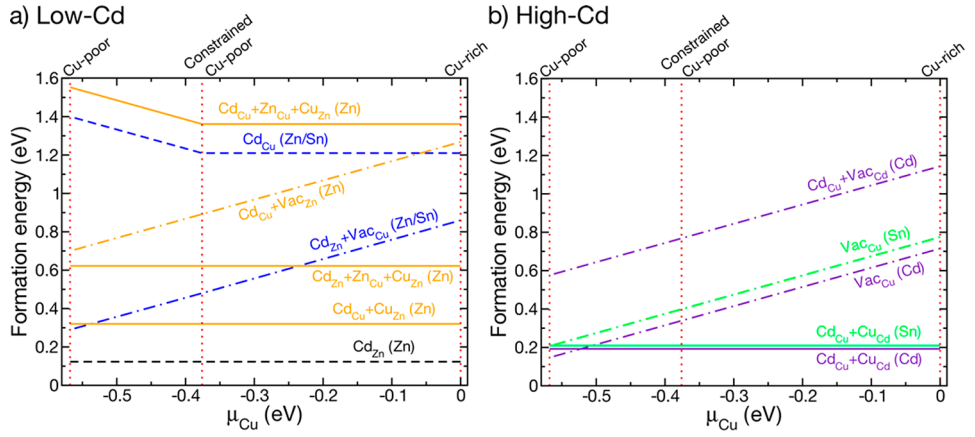

Figure 3. Formation energies, based on DFT-SCAN, of various defects in kesterite Cu_2ZnSnS_4 under (a) a low Cd doping level ($x_{Cd} \sim 0.015$ per S) and (b) a high Cd doping level ($x_{Cd} \sim 0.125$ per S) plotted vs the chemical potential of Cu. The notations "(Sn)", "(Zn)", and "(Cd)" indicate defects occurring on the Sn, Zn, and Cd planes of the kesterite structure (Figure 1), respectively. Vac indicates vacancy.

red lines in Figure 2)], in agreement with previous calculations employing GGA.[11] The chemical potential for the constrained Cu-poor region, pinning the Zn and Sn chemical potentials to ZnS and SnS, respectively (see Methods), is $\mu_{Cu} = -0.38$ eV. Note that the constrained Cu-poor term represents the chemical potential of Cu for synthesis of Cu_2ZnSnS_4 under Cu-poor, Zn-rich, and Sn-rich conditions.

The formation energies for the Cu_{Zn}+Zn_{Cu} antisites (solid lines) across μ_{Cu} in Figure 2 are ~0.22 and ~0.25 eV for the Zn and Sn planes, respectively. These low values indicate that the kesterite structure is likely to exhibit disorder irrespective of the Cu content during synthesis, in agreement with previous studies.[11,20,21,24] Indeed, a defect formation of energy of ~0.2 eV in a given semiconductor can correspond to a substantial concentration of $\sim 2.2 \times 10^{19}$ cm^{-3} at 298 K.[50,69] Additionally, defect concentrations of $\sim 10^{15}$ cm^{-3} (or above) in semiconductors can be measured by experiments.[70]

The ease of forming Cu vacancies increases, as expected, with decreasing Cu availability within kesterite. This is indicated by the linear decrease in the formation energy of Vac_{Cu} (dashed orange and green lines in Figure 2), with a decrease in μ_{Cu}. For example, the formation energy of Vac_{Cu} on the Sn plane (dashed green line) decreases linearly from ~0.74 eV at $\mu_{Cu} = 0$ eV to ~0.17 eV at $\mu_{Cu} = -0.57$ eV. Also, the trends in Vac_{Cu} formation energies are roughly identical in both Sn and Zn planes. Interestingly, the ease of Zn vacancy formation (dashed black line in Figure 2) also increases with decreasing in μ_{Cu}. Indeed, the formation energy of Vac_{Zn} decreases gradually from ~1.17 eV at $\mu_{Cu} = 0$ eV (Cu-rich) to ~0.79 eV at $\mu_{Cu} = -0.38$ eV (constrained Cu-poor) and decreases dramatically (~0.41 eV) under Cu-poor conditions ($\mu_{Cu} = -0.57$ eV).

Cd Doping. Defect formation energies (for neutral defects) are plotted against the Cu chemical potential in kesterite Cu_2ZnSnS_4 at a low Cd doping level ($x_{Cd} \sim 0.015$ per S; panel a) and a high Cd doping level ($x_{Cd} \sim 0.125$ per S; panel b). At a low Cd doping level, a Zn or Cu site is replaced by a Cd atom, while half of the available Zn sites in the kesterite are replaced with Cd at high Cd doping levels. Note that both Zn sites within a kesterite unit cell are equivalent, and replacing either of the Zn sites with a Cd atom will be equivalent in energy. Thus, all Zn sites in alternate Zn planes within the kesterite structure (Figure 1a) are occupied by Cd at high Cd doping levels, leading to the formation of distinct Zn and Cd planes. In a supercell, Zn/Cd arrangements different from the distinct Zn and Cd plane ordering considered here could occur; however, modeling all possible Zn/Cd decorations is prohibitively expensive. As in Figure 2, the notations "(Sn)", "(Zn)", and "(Cd)" in Figure 3 indicate defects occurring on the Sn, Zn, and Cd planes, respectively. Also, the notation "(Sn/Zn)" in Figure 3a indicates that the defect energetics are identical on both a Sn plane and a Zn plane. Dashed lines in Figure 3a indicate the ease of doping Cd on a Cu (Cd_{Cu}) or Zn (Cd_{Zn}) site. Dash−dot lines in both panels of Figure 3 indicate the formation of a vacancy that neighbors a Cd atom. For example, Cd_{Zn}+Vac_{Cu} (Zn/Sn) in Figure 3a (blue dash−dot line) indicates the formation of a Cu vacancy on either the same Zn plane or an adjacent Sn plane that neighbors a doped Cd atom on a Zn site. Similarly, Vac_{Cu} (Sn) in Figure 3b (green dash−dot line) indicates a Cu vacancy on a Sn plane adjacent to a Cd plane. Solid lines in panels a and b of Figure 3 indicate antisites that can lead to disorder in the Cu and Zn sublattices of the kesterite structure. For example, Cd_{Cu}+Cu_{Zn} (Zn) in Figure 3a indicates a disorder in the Cu and Zn sublattices via Cd and Cu occupation, respectively. Here, (Zn) indicates that the Cd_{Cu} antisite occurs on a Cu site and on a Zn plane. Analogously, Cd_{Zn}+Zn_{Cu}+Cu_{Zn} (Zn) indicates an exchange of Cu and Zn atoms on the same Zn plane that are adjacent to a Cd atom doped on a Zn site.

Across Cu chemical potentials, Cd_{Zn} [~0.12 eV (dashed black line in Figure 3a)] has a formation energy that is lower than that of Cd_{Cu} [~1.21−1.4 eV (dashed blue line)], indicating a facile doping of Cd on Zn sites instead of Cu in the kesterite structure. This strong preference for isovalent substitution is expected and agrees with experimental observations of isovalent-doped inorganic compounds.[71] Note that isolated Cd_{Cu} antisites are not expected to be found at low Cd concentrations, based on their high formation energy (~1.21−1.4 eV). Thus, n-type Cd_{Cu} antisites can occur only in combination with other antisites, such as a charge-compensating p-type Cu_{Zn} defect [solid orange line at ~0.32 eV (Figure 3a)]. A Cd_{Cu}+Cu_{Zn} combination also represents disorder within the Cu and Zn sublattices. In comparison to that of pure Cu_2ZnSnS_4, the energy required to form disorder-inducing antisites is higher at low Cd doping levels (solid orange lines in Figure 3a vs solid lines in Figure 2), indicating suppression of disorder in Cu_2ZnSnS_4. This is in agreement with the experimental observation of higher efficiencies and V_{oc}

DOI: 10.1021/acs.chemmater.8b00677
Chem. Mater. 2018, 30, 4543−4555

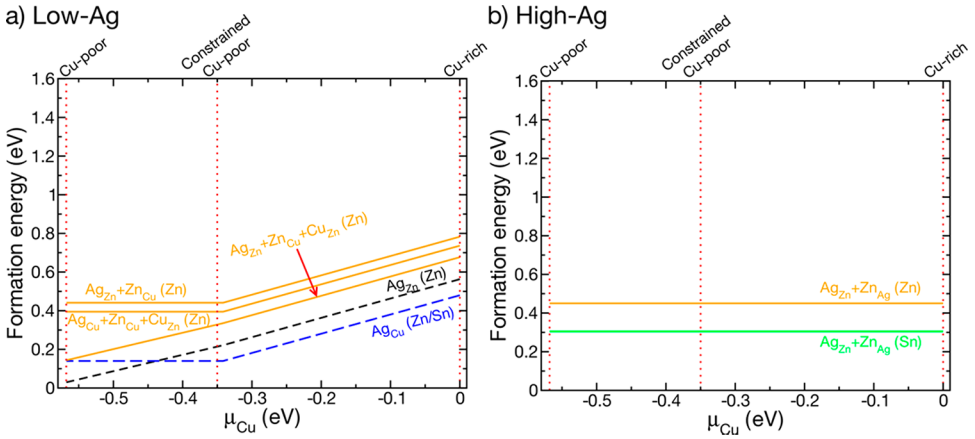

Figure 4. Formation energies, based on DFT-SCAN, of various defects in kesterite Cu_2ZnSnS_4 at (a) a low Ag doping level ($x_{Ag} \sim 0.015$ per S) and (b) a high Ag doping level ($x_{Ag} \sim 0.25$ per S) plotted vs the chemical potential of Cu. The notations "(Sn)" and "(Zn)" indicate defects occurring on the Sn and Zn planes of the kesterite structure (Figure 1), respectively. Vac indicates vacancy.

values in low-Cd-doped cells.[30] Specifically, the formation energies of $Cd_{Cu}+Cu_{Zn}$ (Zn), $Cd_{Zn}+Zn_{Cu}+Cu_{Zn}$ (Zn), and $Cd_{Cu}+Zn_{Cu}+Cu_{Zn}$ (Zn) (solid orange lines in Figure 3a) are ~0.32, 0.62, and 1.36−1.55 eV, respectively, all higher than the energy required to induce disorder in undoped Cu_2ZnSnS_4 [0.22−0.25 eV (solid lines in Figure 2)]. Also, the ease of forming a Cu vacancy adjacent to a doped Cd atom [$Cd_{Zn}+Vac_{Cu} \sim 0.29-0.86$ eV (dash−dot blue line in Figure 3a)] is similar to that of forming a Cu vacancy adjacent to a Zn atom in pure Cu_2ZnSnS_4 [~0.18−0.75 eV (Figure 2)]. Cd doping therefore leaves the favorability of Vac_{Cu} formation unchanged while suppressing disorder. Additionally, Zn vacancies are less likely to form in Cd-doped Cu_2ZnSnS_4 than in pristine kesterite, indicated by the high formation energies of $Cd_{Cu}+Vac_{Zn}$ (Zn) [~0.7−1.27 eV (dashed orange line in Figure 3a)].

Interestingly, Cd ceases to suppress the formation of antisites in the kesterite structure at high levels of doping, as indicated by the solid lines in Figure 3b. Indeed, the energies to disorder via the creation of $Cd_{Cu}+Cu_{Cd}$ (Cd) and $Cd_{Cu}+Cu_{Cd}$ (Sn) are ~0.19 and 0.21 eV, respectively, lower than the energy required to disorder the undoped kesterite [~0.22−0.25 eV (Figure 2)]. Thus, high levels of Cd within the kesterite will produce a higher degree of disorder, resulting in lower V_{oc} values and efficiencies, again consistent with experimental observations.[30] However, a high Cd content within the kesterite can induce Vac_{Cu} in the Cd and Sn planes, especially under constrained Cu-poor to Cu-poor conditions. This is indicated by the low formation energies (~0.15−0.4 eV for Vac_{Cu} for those conditions in Figure 3b), which might mitigate potential decreases in efficiency.

Ag Doping. Formation energies for various (neutral) defects in kesterite Cu_2ZnSnS_4 at a low Ag doping level ($x_{Ag} \sim 0.015$ per S; panel a) and a high Ag doping level ($x_{Ag} \sim 0.25$ per S; panel b) are plotted against the Cu chemical potential in Figure 4. Note that the chemical potential corresponding to constrained Cu-poor conditions has a slightly different value ($\mu_{Cu} = -0.35$ eV) in the Ag−Cu−Zn−Sn−S quinary system compared to those in the Cu−Zn−Sn−S quaternary and Cd−Cu−Zn−Sn−S quinary systems ($\mu_{Cu} = -0.38$ eV). Analogous to the case with Cd doping (Figure 3), either a Cu or Zn site is replaced with a Ag atom at low Ag doping levels within the kesterite, while half of the Cu atoms are replaced with Ag at high Ag doping levels. Notably, there are three different ways to replace half of the Cu sites with Ag within a kesterite unit cell, namely, (i) replace two Cu sites on a Sn plane with Ag, (ii) replace two Cu sites on a Zn plane with Ag, and (iii) replace one Cu atom in each of two adjacent Zn and Sn planes with Ag. We calculated all of the aforementioned configurations, i.e., substituting Cu sites with Ag, and found that the energy cost to replace two Cu sites on a Sn plane with Ag is the lowest (lower than those of the two other configurations considered by ~11 meV/f.u.). This finding leads to the formation of distinct Sn−Ag and Zn−Cu planes within the kesterite lattice. As a result, we used the configuration of replacing two Cu sites on a Sn plane with Ag for further calculations of defect energetics at high Ag doping levels (Figure 4b). As in the case of Cd doping, we do not consider all possible Cu/Ag orderings within supercells of Cu_2ZnSnS_4. The notations "(Sn)" and "(Zn)" used in Figure 4 indicate defects occurring on the Sn and Zn planes, respectively, similar to the notations used in Figures 2 and 3. Note that at high Ag doping levels (Figure 4b), "(Sn)" and "(Zn)" refer to the Sn−Ag and Zn−Cu planes, respectively. "(Zn/Sn)" in Figure 4a also indicates that the defect energetics are identical on both a Zn plane and a Sn plane. Dashed lines in Figure 4a indicate the ease of doping Ag on a Cu (Ag_{Cu}) or Zn (Ag_{Zn}) site. Solid lines in Figure 4 indicate antisites that lead to disorder in the kesterite structure. For example, $Ag_{Zn}+Zn_{Cu}$ (Zn) corresponds to the Ag and Zn occupations of Zn and Cu sites, respectively, on a Zn plane, signifying disorder.

Doping Ag on Cu sites is more energetically favored under Cu-rich and constrained Cu-poor conditions in Figure 4a [~0.14−0.48 eV (dashed blue line in Figure 4a)] than doping Ag on Zn sites [~0.22−0.56 eV (dashed black line)]. However, under Cu-poor conditions ($\mu_{Cu} < -0.4$ eV), Ag doping on Zn sites becomes more facile (~0.03 eV at $\mu_{Cu} = -0.57$ eV) compared to Ag doping on Cu sites (~0.14 eV). Doping low levels of Ag in Cu_2ZnSnS_4 therefore is quite sensitive to the Cu conditions present during synthesis. With regard to introducing disorder in the lattice at low doping levels, Ag is effective at suppressing antisite formation only under constrained Cu-poor to Cu-rich conditions, as indicated by the formation energies of three antisite combinations (in the range of -0.35 eV $\leq \mu_{Cu} \leq 0$ eV) that represents disorder in the kesterite structure: (i) $Ag_{Zn}+Zn_{Cu}+Cu_{Zn}$ (Zn), ~0.34−

DOI: 10.1021/acs.chemmater.8b00677
Chem. Mater. 2018, 30, 4543−4555

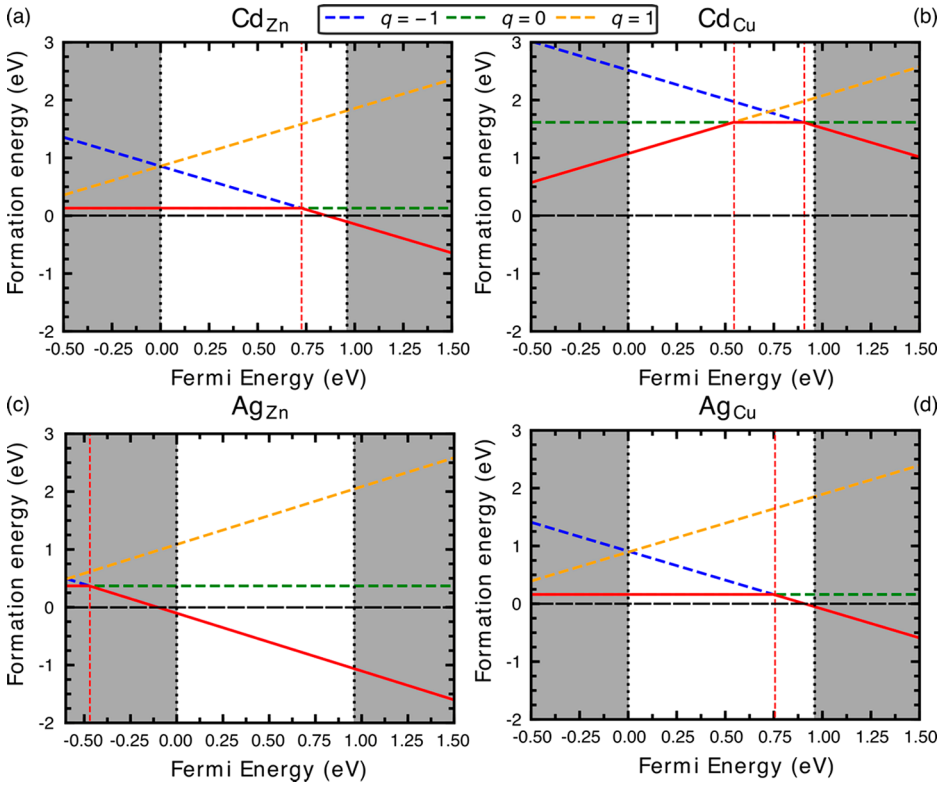

Figure 5. Formation energies of various charged antisites considered within kesterite Cu_2ZnSnS_4, including (a) Cd_{Zn}, (b) Cd_{Cu}, (c) Ag_{Zn}, and (d) Ag_{Cu}, plotted as a function of the Fermi energy. The shaded gray regions indicate the valence band (Fermi energy of <0), and the conduction band (Fermi energy of >0.96 eV), where the zero of the Fermi energy is arbitrarily set to the valence band maximum. Three ionized states are considered for each antisite, namely, $q = -1$ (negatively charged, dashed blue), $q = 0$ (neutral, dashed green), and $q = 1$ (positively charged, dashed orange). The solid red line in each plot indicates the minimum formation energy at each Fermi energy, indicative of the most stable charged state of the defect. Dashed red vertical lines signify acceptor (q, $0 \rightarrow -1$) and/or donor (q, $1 \rightarrow 0$) transition levels. All charged defect calculations are performed using the GGA+U+D functional.

0.68 eV; (ii) Ag_{Cu}+Zn_{Cu}+Cu_{Zn}, ∼0.39−0.74 eV; and (iii) Ag_{Zn}+Zn_{Cu} (Zn), ∼0.44−0.78 eV. Under Cu-poor conditions, a low Ag concentration favors disorder in the Cu_2ZnSnS_4 lattice in comparison to undoped Cu_2ZnSnS_4 (Figure 2), as indicated by the low formation energy of Ag_{Zn}+Zn_{Cu}+Cu_{Zn} (Zn) (∼0.14 eV) and Ag_{Zn} (∼0.03 eV). A low Ag doping level therefore is most effective at inhibiting disorder and improving efficiency in the kesterite structure only under constrained Cu-poor to Cu-rich conditions. This is in contrast to a low Cd doping level (Figure 3a), which inhibits lattice disorder under all Cu conditions.

At high levels of Ag doping in the lattice (Figure 4b), the formation of antisite defects, namely Ag_{Zn}+Zn_{Ag}, becomes insensitive to Cu chemical potential. Also, given the higher formation energies of Ag_{Zn}+Zn_{Ag} (∼0.45 and 0.30 eV on the Zn and Sn planes, respectively) compared to that of undoped Cu_2ZnSnS_4 [∼0.22−0.25 eV (Figure 2)], Ag should inhibit disorder in the kesterite structure at high Ag concentrations. Note that the suppression of disorder at high levels of Ag doping is in contrast to the behavior displayed by Cd (Figure 3b).

Charged Defects in Doped Cu_2ZnSnS_4. To understand the impact of Cd or Ag doping on the intrinsic hole conductivity[23] of Cu_2ZnSnS_4, we consider the stability of various charged configurations of the lowest-energy antisites, namely, Cd_{Zn} (Figure 3a), Ag_{Zn}, and Ag_{Cu} (Figure 4a). We also consider ionized configurations of Cd_{Cu} antisites to facilitate a direct comparison with Cd_{Zn}. Note that only at low dopant concentrations can ionized dopants influence hole (or electron) conductivity without altering the bulk electronic structure. Hence, we consider ionized antisites in Cu_2ZnSnS_4 at only a low Cd or Ag doping level (x_{Cd} or $x_{Ag} \sim 0.015$ per S). Because we perform all charged defect calculations using the GGA+U+D functional, we consider the stability of ionized defects only under Cu-poor conditions.

Figure 5 plots the formation energies of Cd_{Zn} (panel a), Cd_{Cu} (panel b), Ag_{Zn} (panel c), and Ag_{Cu} (panel d) antisites as a function of the Fermi energy, which is arbitrarily set to 0 eV at the valence band maximum of kesterite Cu_2ZnSnS_4. The shaded gray regions in Figure 5 represent the valence (Fermi energy of <0 eV) and conduction [Fermi energy of >0.96 eV, the predicted band gap of kesterite Cu_2ZnSnS_4 (Figure S2a)] bands. Dashed blue, green, and orange lines in all panels indicate negatively charged ($q = -1$), neutral ($q = 0$), and positively charged ($q = 1$) defects, respectively. Solid red lines in each panel signify the lowest-energy charge state for the corresponding defect. For example, the neutral ($q = 0$) Cd_{Zn} antisite (panel a) is stable up to a Fermi energy of ∼0.73 eV, beyond which the negatively charged ($q = -1$) defect becomes stable. Dashed red lines in Figure 5 indicate donor and/or acceptor transition levels. For example, in the case of donor defects [Cd_{Cu} (Figure 5b)], the excess electron can either localize on the donor site ($q = 0$) or be exchanged with the electron reservoir of the structure, whose energy equals the Fermi energy ($q = 1$). Thus, a donor transition level (q, $1 \rightarrow 0$) corresponds to the Fermi energy at which the neutral and

DOI: 10.1021/acs.chemmater.8b00677
Chem. Mater. 2018, 30, 4543−4555

positively charged defect states have equal formation energies. Similarly, for acceptor defects, the excess hole can either localize on the acceptor site ($q = 0$) or be exchanged with the hole reservoir, whose energy equals the Fermi energy ($q = -1$). An acceptor transition level [e.g., Ag_{Zn} (Figure 5c)] is the Fermi energy at which the neutral and negatively charged defect states have equal energies (q, $0 \rightarrow -1$). Notably, if a donor (acceptor) transition level is "shallow", i.e., the transition level lies $\approx k_B T$ from the conduction (valence) band edge, thermal ionization leading to free electrons (holes) can occur, resulting in significant improvement in electron (hole) conductivity. Analogously, "deep" transition levels ($\gg k_B T$ from the band edges) do not lead to an enhancement in carrier conductivity and often result in the formation of trap states, facilitating nonradiative carrier recombination.

Isovalent antisites, namely, Cd_{Zn} (Figure 5a) and Ag_{Cu} (Figure 5d), exhibit deep acceptor transition levels, at ~0.73 eV (Cd_{Zn}) and ~0.76 eV (Ag_{Cu}), with the corresponding $q = 0$ and $q = 1$ charged states exhibiting the lowest and highest formation energies, respectively, over most Fermi energies across the band gap. Thus, both isovalent antisites are not expected to significantly contribute to the hole conductivity in kesterite Cu_2ZnSnS_4. However, given their low formation energies (~0.13−0.16 eV), isovalent antisites can lead to the formation of deep hole traps, potentially resulting in enhanced hole−electron recombination and reduced performance. Interestingly, Cd_{Cu}, which is a donor defect, exhibits both a deep donor transition (at a Fermi energy of ~0.54 eV) and a deep acceptor transition (~0.91 eV) within the band gap. However, given the high formation energies (>1 eV within the band gap) and the deep transition levels, Cd_{Cu} is not expected to significantly contribute to either electron or hole conductivity within Cu_2ZnSnS_4. Notably, a comparison of the formation energies of the positively charged Cd_{Cu} (dashed orange in Figure 5b) and the neutral Cd_{Zn} (dashed green in Figure 5a), both of which correspond to an identical number of electrons within the kesterite structure, indicates that at low Cd doping levels (and under Cu-poor conditions), Cd will always occupy Zn sites, in qualitative agreement with our neutral defect calculations (Figure 3a).

Surprisingly, the acceptor Ag_{Zn} antisite (Figure 5c) exhibits (i) an acceptor transition within the valence band (~−0.47 eV) and (ii) a negative formation energy across the band gap, indicating that the ionized ($q = -1$) Ag_{Zn} will remain thermodynamically stable at low Ag doping levels and under Cu-poor conditions. Although GGA+U calculations have well-documented shortcomings with respect to their quantitative accuracy for defect formation energies,[50] qualitative trends are typically reliable. Thus, our calculations do indicate spontaneous ionization of Ag_{Zn} antisites resulting in a substantial increase in free hole concentration (and conductivity) with a low Ag doping level in Cu_2ZnSnS_4. However, large increases in free hole concentration can also result in metallic-like behavior of the Ag-doped kesterite, which might be deleterious for maintaining a reasonable V_{oc} and PV efficiency. Also, a comparison of the formation energies of neutral Ag_{Cu} and negatively charged Ag_{Zn} (both of which possess an identical number of electrons) indicates that a low Ag doping level under Cu-poor conditions will always lead to preferential Ag occupation of Zn sites. Given that the formation energy of neutral Ag_{Zn} is higher than that of Ag_{Cu} under constrained Cu-poor and Cu-rich conditions (Figure 4a), Ag is more likely to occupy Cu sites (and form neutral antisites) under higher Cu chemical potentials, indicating the importance of Cu conditions during the synthesis and operation of Ag-doped Cu_2ZnSnS_4.

Bulk Stabilities, Band Gaps, and Surface Energetics. The energy difference between the stannite and kesterite polymorphs (in eV/f.u.), calculated using DFT-SCAN, is displayed in Figure 6 for undoped (red bar), fully Cd-doped (purple), and fully Ag-doped (blue) Cu_2ZnSnS_4. Positive values of the energy difference indicate that the kesterite structure is more stable than the stannite. The dashed purple (white) line indicates the energy difference between the two polymorphs at a composition of $Cu_2Zn_{0.5}Cd_{0.5}SnS_4$ ($CuAgZnSnS_4$). In undoped Cu_2ZnSnS_4 (red bar in Figure 6), the kesterite structure is marginally more stable than the stannite structure (~28 meV/f.u.), in agreement with previous theoretical estimates using GGA+U.[21] Cd substitution stabilizes the stannite structure, with energy differences of approximately 11 and −29 meV/f.u. at $Cu_2Zn_{0.5}Cd_{0.5}SnS_4$ and Cu_2CdSnS_4, respectively, with both values being lower than that of undoped Cu_2ZnSnS_4 (~28 meV/f.u.). The stannite structure therefore becomes more stable than the kesterite when all Zn atoms in Cu_2ZnSnS_4 are replaced with Cd. In the case of Ag doping, increasing replacement of Cu with Ag increases the stability of the kesterite polymorph, as indicated by energy differences of approximately 31 and 157 meV/f.u. at $CuAgZnSnS_4$ (dashed white line) and Ag_2ZnSnS_4 (purple bar), respectively.

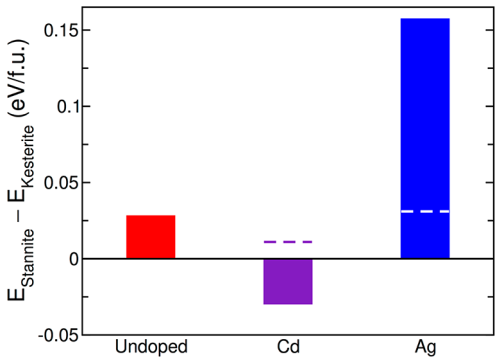

Figure 6. Stability of the stannite structure, calculated using DFT-SCAN, with respect to the kesterite structure for undoped Cu_2ZnSnS_4 (red bar), Cu_2CdSnS_4 (purple), and Ag_2ZnSnS_4 (blue). The dashed purple and white lines indicate the energy difference between the stannite and kesterite structures for $Cu_2Cd_{0.5}Zn_{0.5}SnS_4$ and $CuAgZnSnS_4$, respectively.

Figures S2 (panels a and b) and S3 display the total density of states in pristine and doped Cu_2ZnSnS_4, respectively, for both the kesterite and stannite polymorphs, as obtained via GGA+U+D calculations. Note that band gaps obtained from GGA+U+D calculations are reliable only for qualitative comparisons with experimental trends.[72] For a quantitative comparison, screened one-particle Green's function (GW) calculations need to be employed[73] but are prohibitively expensive for the unit cell sizes used in our calculations. For undoped Cu_2ZnSnS_4, the band gaps of both the kesterite [~0.96 eV (Figure S2a)] and the stannite [~0.79 eV (Figure S2b)] structures are in agreement with previous calculations.[23] Cd and Ag substitutions in Cu_2ZnSnS_4 affect the band gaps of both the kesterite and stannite lattices in contrasting ways. Specifically, band gaps of both kesterite and stannite

DOI: 10.1021/acs.chemmater.8b00677
Chem. Mater. 2018, 30, 4543−4555

Cu_2CdSnS_4, namely, ∼0.76 and ∼0.75 eV, respectively (Figure S3a,b), are marginally lower than that of undoped Cu_2ZnSnS_4 (Figure S2a,b), similar to experimental trends.[74] By contrast, Ag substitution increases the band gaps of both kesterite [∼1.27 eV (Figure S3c)] and stannite Ag_2ZnSnS_4 [∼0.94 eV (Figure S3d)] compared to that of Cu_2ZnSnS_4, also similar to experimental observations.[75]

Table 2 shows the change in surface energy (or relative surface energy, $\Delta E_{surface}^{doped} = E_{surface}^{doped} - E_{surface}^{pristine}$) with Cd and Ag doping for the (110) and (112) surfaces in the kesterite structure. Relative surface energies can indicate the (de)-stabilization of a given surface caused by doping and are referenced to the energies of the corresponding surfaces in undoped kesterite Cu_2ZnSnS_4 in Table 2. For calculating the Cd- and Ag-doped surface energies, we consider the GGA+*U*+*D* relaxed bulk structures of kesterite $Cu_2Zn_{0.5}Cd_{0.5}SnS_4$ and $CuAgZnSnS_4$, respectively. We consider the (110) and (112) surfaces for our calculations, because previous experiments found that the aforementioned surfaces are dominant during particle growth of kesterite Cu_2ZnSnS_4.[30,33] Note that the stoichiometric (112) surface is not charge-neutral but is a type 3 surface, according to the classification system of Tasker,[76] which necessitates creation of antisite defects (such as two Zn_{Sn}) to ensure charge neutrality.[59] The stoichiometric (112) surface has four excess electrons, as deduced by electron counting rules,[62] which can be compensated for by defects, such as two Zn_{Sn}, Cu_{Sn}+Cu_{Zn}, Vac_{Sn}, two Vac_{Cu}+Vac_{Zn}, etc. We chose the two Zn_{Sn} antisites to estimate the impact of doping on surface energetics under the Zn-rich conditions often desired during Cu_2ZnSnS_4 synthesis.[20,24] Each (110) plane in the kesterite structure has either Zn+Cu atoms (Zn planes) or Sn+Cu atoms (Sn planes), as well. We chose the Zn+Cu termination for our analysis here (denoted "Zn-terminated" in Table 2), because Cd_{Zn} defects favorably form in the Zn planes of the kesterite (dashed black line in Figure 3); any influence of Cd doping on surface energetics will be strongest on Zn+Cu planes.

Table 2. Changes in Surface Energy (calculated using GGA+*U*+*D*) upon Cd and Ag Doping, As Referenced to the Corresponding Surface Energy of Undoped Kesterite Cu_2ZnSnS_4, for the (110) and (112) Surfaces[a]

surface	$\Delta E_{surface}^{Cd\text{-}doped}$ (J/m^2)	$\Delta E_{surface}^{Ag\text{-}doped}$ (J/m^2)
(110), Zn-terminated	0.016	−0.242
(112), two Zn_{Sn} antisites	−0.001	−0.376

[a]We consider a (110) surface with Zn+Cu termination and a (112) surface with two Zn_{Sn} antisites to calculate the surface energies.

Cd doping has a negligible effect on surface energetics, with changes in energy of ∼16 and ∼1 mJ/m^2 for the (110) and (112) surfaces, respectively. In comparison to the GGA+*U*+*D* cleavage energies reported previously,[21] the percentage changes in (110) and (112) surfaces with Cd doping are a mere ∼2 and ∼0.1%, respectively, indicating that Cd doping should not affect particle growth or morphology during synthesis. Ag doping affects the surface energies more significantly than Cd doping does, stabilizing the (110) and (112) surfaces by ∼242 and ∼376 mJ/m^2, respectively, with respect to undoped Cu_2ZnSnS_4. In terms of the percentage change with respect to cleavage energies,[21] Ag doping causes ∼31 and ∼48% decreases in surface energies of the (110) and (112) surfaces, respectively. A significant decrease in surface energy nominally should correspond to a reduced particle size during synthesis. However, experiments reveal only the opposite, namely significant particle coarsening in Ag-doped samples,[31,33] suggesting that Ag plays a more significant role via bulk and defect (Figures 4 and 5) rather than surface energetics. Additionally, the high-temperature-annealing conditions employed during selenization of Cu_2ZnSnS_4[26,77] probably overcome the driving force for particle-size reduction in Ag-doped Cu_2ZnSnS_4, leading to particle coarsening.

DISCUSSION

Kesterite Cu_2ZnSnS_4, an important candidate light absorber for beyond-Si solar cells, exhibits significant disorder in the Cu and Zn sublattices,[20,21,23] leading to poor efficiencies of Cu_2ZnSnS_4-based solar cells.[10] Isovalent doping on the Cu^+ and Zn^{2+} sublattices has been proposed as a potential strategy for suppressing cation disorder within the kesterite structure.[27,28] Indeed, experiments involving Ag^+ and Cd^{2+} doping within Cu_2ZnSnS_4 have reported improved performance,[30,31] albeit at intermediate dopant concentrations. Hence, it is important to understand the fundamental role of dopants within Cu_2ZnSnS_4 and to identify limitations, if any. Here, we performed in-depth, first-principles quantum mechanics calculations to assess the influence of Cd and Ag doping on bulk stability, defect and surface energetics, and electronic structure, at low and high levels of Cd and Ag doping. We find that both Cd and Ag can suppress disorder and improve the efficiency of kesterite Cu_2ZnSnS_4-based solar cells, at select doping levels and under Cu conditions during synthesis. We also determine at low doping concentrations that the constrained Cu-poor condition, which corresponds to the constraint of including Cu-poor, Zn-rich, and Sn-rich conditions during Cu_2ZnSnS_4 synthesis, is ideal for minimizing cation disorder within the kesterite structure.

In the case of Cd doping, Cd clearly prefers the occupation of Zn over Cu sites in the kesterite structure, as indicated by the lower formation energy for neutral Cd_{Zn} antisites [∼0.12 eV (Figure 3a)] rather than for neutral Cd_{Cu} antisites (∼1.21−1.4 eV). The tendency of Cd to occupy Zn sites is further validated by the higher formation energy of positively charged Cd_{Cu} [>1 eV (Figure 5b)], which corresponds to an identical number of electrons in the lattice as that of neutral Cd_{Zn} [∼0.13 eV (Figure 5a)]. Importantly, Cd inhibits disorder only at low doping concentrations, as indicated by the higher energy cost to form disordering neutral antisites [∼0.32−0.62 eV (Figure 3a)] rather than undoped Cu_2ZnSnS_4 [∼0.22−0.25 eV (Figure 2)]. In addition, a low Cd doping level is not expected to enhance the hole conductivity of kesterite Cu_2ZnSnS_4 because of the deep acceptor transition level of both Cd_{Zn} and Cd_{Cu} antisites (Figure 5a,b). At a higher Cd content, the stannite structure becomes increasingly stable (purple bar in Figure 6) alongside an increasing tendency of the kesterite to disorder [∼0.19−0.21 eV (Figure 3b)]. Additionally, Cd doping is expected to decrease the overall band gap of both the kesterite and stannite polymorphs (Figure S3a,b). Thus, the contrasting behavior of Cd at low and high doping levels indicates that there will be a specific, low Cd concentration at which Cu_2ZnSnS_4 will achieve peak efficiency and V_{oc}, in agreement with experimental observations of maximum efficiency at ∼5% Cd doping.[30]

In Ag-doped Cu_2ZnSnS_4, the site preference of Ag is sensitive to the chemical potential of Cu within the kesterite structure. For example, under Cu-poor conditions, Ag^+ can be

DOI: 10.1021/acs.chemmater.8b00677
Chem. Mater. 2018, 30, 4543−4555

doped either on Cu^+ (isovalent antisite) or on Zn^{2+} (p-type) sites, as indicated by comparable neutral Ag_{Cu} [~0.14 eV (Figure 4a)] and neutral Ag_{Zn} (~0.03 eV) formation energies. Doping of Ag within Cu_2ZnSnS_4 therefore is highly sensitive to Cu conditions during synthesis. Additionally, at low Ag doping levels and especially under Cu-poor conditions, Ag does not suppress cation disorder within the kesterite structure, as indicated by the low formation energy of disorder-inducing neutral antisites [~0.14 eV (Figure 4a)] compared to that of undoped Cu_2ZnSnS_4 [~0.22−0.25 eV (Figure 2)]. Furthermore, Ag_{Zn}, which is an acceptor antisite, can spontaneously ionize within the kesterite structure under Cu-poor conditions (negative formation energies in Figure 5c), potentially leading to large increases in the concentration of free holes. Note that low Ag doping levels can suppress disorder at higher Cu chemical potentials [~0.34−0.78 eV from constrained Cu-poor to Cu-rich conditions (Figure 4a)]. Also, Ag_{Cu} antisites, which are the most likely defect under Cu-rich conditions, will not contribute significantly to the hole conductivity of the kesterite because of its deep acceptor transition level (Figure 5d). Thus, low levels of Ag doping may not be an effective strategy for improving the performance of Cu_2ZnSnS_4 cells because Ag requires Cu-rich conditions to suppress disorder, which disfavors the formation of Vac_{Cu} and the subsequent retention of p-type behavior in Cu_2ZnSnS_4. Notably, Ag substitution in Cu_2ZnSnS_4 stabilizes the kesterite structure (blue bar in Figure 6), in addition to increasing the band gap of both the kesterite and stannite polymorphs (Figure S3c,d). Altogether, increased disorder at low Ag concentrations versus an increased band gap in kesterite may be the origin of the peak efficiency and V_{oc} typically observed in low-Ag-doped samples.[31] Interestingly, Ag is more effective at reducing disorder in the kesterite at higher Ag concentrations within the structure, as indicated by higher formation energies of disorder inducing neutral antisites [~0.30−0.45 eV (Figure 4b)], across Cu chemical potentials. Hence, the effectiveness of Ag in improving the efficiency of a Cu_2ZnSnS_4-based solar cell will be highly dependent on the synthesis conditions, specifically on the concentration of Ag being doped and the Cu content used during synthesis.

Our results indicate that Cd doping and Ag doping have contrasting influences on the bulk stability, defect energetics, and electronic properties of kesterite Cu_2ZnSnS_4 and result in performance improvements via different mechanisms. For example, across a range of Cu conditions, disorder in the Cu and Zn sublattices is inhibited only at low (high) levels of Cd (Ag) doping in the kesterite. Similarly, high levels of Cd and Ag stabilize the stannite and kesterite polymorphs, respectively (Figure 6). Cd (Ag) doping also is expected to decrease (increase) the band gap of both kesterite and stannite (Figure S3). Coincidentally, at low levels of doping, both Cd and Ag inhibit lattice disorder within kesterite under constrained Cu-poor conditions. This is in qualitative agreement with experimental observations of maximum efficiency resulting from using Cu-poor, Zn-rich, and Sn-rich conditions during Cu_2ZnSnS_4 synthesis.

Interestingly, Cd and Ag stabilize different polymorphs (Figure 6) despite both ions being isovalent dopants (on Zn and Cu, respectively) and being significantly larger than the ions they replace, which may be attributed to a combination of electrostatic and steric effects. For example, the kesterite polymorph is electrostatically favored at the Cu_2ZnSnS_4 composition, as indicated by an electrostatic energy (~−353.2 eV, calculated via the Ewald summation technique[78]) that is lower than that of the stannite polymorph (−352.6 eV). Most of the electrostatic stabilization of kesterite arises from weaker repulsions between intralayer Sn^{4+}−Cu^+ compared to Sn^{4+}−Zn^{2+} in stannite. In terms of steric interactions, neighboring atoms of a similar size lead to less steric strain than atoms of significantly different sizes. Thus, the stannite is better at accommodating steric strain because identical Cu^+ ions (or Ag^+ in stannite Ag_2ZnSnS_4) occupy the same (001) plane (Figure 1b). In Cu_2CdSnS_4, the intralayer Sn^{4+}−Cd^{2+} distance in stannite is larger (~3.94 Å, after structural relaxation using DFT-SCAN) than the Sn^{4+}−Zn^{2+} distance (~3.81 Å) in stannite Cu_2ZnSnS_4. The larger Sn^{4+}−Cd^{2+} distance decreases the level of electrostatic repulsion, which, in combination with the favorable steric interactions of planar Cu^+ segregation, stabilizes the stannite polymorph at high Cd levels. In the case of kesterite Ag_2ZnSnS_4, both intralayer Sn^{4+}−Ag^+ and Zn^{2+}−Ag^+ distances (~4.1 Å) are significantly larger than Sn^{4+}−Cu^+ and Zn^{2+}−Cu^+ distances in kesterite Cu_2ZnSnS_4 (~3.81 Å). By contrast, both Sn^{4+}−Zn^{2+} and Ag^+−Ag^+ distances are smaller (~3.88 Å) in stannite Ag_2ZnSnS_4. Thus, the stabilization of kesterite at high Ag levels can be attributed to weakened electrostatic interactions.

Experiments often measure improved performance in Cu_2ZnSnS_4 solar cells when there is a gradation in Ag content, i.e., higher Ag content toward the n-type CdS layer than toward the bulk Cu_2ZnSnS_4 layer.[32] Cd interdiffusion from the n-CdS layer into the Cu_2ZnSnS_4 lattice may occur during operation, where a high Cd content within Cu_2ZnSnS_4 can detrimentally reduce efficiency and V_{oc}. A high Ag concentration, adjacent to the CdS layer, might help counterbalance the effect of Cd diffusion, stabilizing ordered kesterite and retaining the band gap, thereby improving the performance, explaining experimental trends.[32] Cd doping within bulk Cu_2ZnSnS_4 may also help by inhibiting diffusion of Cd from the CdS layer by decreasing the Cd concentration gradient across the Cu_2ZnSnS_4−CdS interface.

In this work, we have not considered the effect of selenization in combination with Ag or Cd doping in Cu_2ZnSnS_4. Previous experimental studies have shown that conditions employed during the selenization process (~500 °C) can result in particle coarsening of the as-synthesized Cu_2ZnSnS_4.[77] As we do not observe notable changes (0.1−2%) in the energies of the (110) and (112) surfaces of the kesterite with Cd doping, while finding a significant decrease (31−48%) in the (110) and (112) surfaces with Ag doping (Table 2), we speculate that the particle coarsening reported with both Cd and Ag doping (and attributed to dopants)[30,31] is due to the annealing conditions during the selenization process. Notably, substitution of Se for S also leads to an increase in chemical space that is available for $Cu_2ZnSn(S,Se)_4$ to be in equilibrium with or to decompose into, which could change the range of Cu chemical potentials with which the kesterite structure can be in equilibrium. Therefore, significant care must be taken to ensure that undesired side products are not produced during the selenization process.

As one of the main goals in exploring the Cu−Zn−Sn−S chemistry, away from the better performing Cu−In−Ga−S (CIGS) system, is the usage of both abundant and nontoxic elements,[9] both Ag (rare) and Cd (toxic) are not viable dopants for sustainable, beyond-Si solar cell technology. Hence, new abundant, nontoxic, isovalent dopants must be explored. Probable candidates include alkali (Na^+, K^+, etc.)[79]

DOI: 10.1021/acs.chemmater.8b00677
Chem. Mater. 2018, 30, 4543−4555

and alkaline earth (Mg^{2+}, Ca^{2+}, etc.)[80] metals. Aliovalent doping using other 3d transition metals, such as Fe^{3+}, Cr^{3+}, Mn^{2+}, etc., may also be explored.[81] The framework used in this work therefore can be extended for the identification of promising dopants to improve the performance of Cu_2ZnSnS_4 solar cells.

CONCLUSIONS

We employed first-principles quantum mechanics calculations to understand the role of Cd and Ag doping in improving the performance of kesterite Cu_2ZnSnS_4, a promising, cheap, beyond-Si solar cell material. On the basis of our calculations of bulk stability, defect energetics, and electronic properties, we find that Cd doping and Ag doping result in improved V_{oc} and efficiency via contrasting mechanisms. Low levels of Cd doping can suppress disorder in the Cu−Zn sublattice, as indicated by the increased formation energies of antisite defects, while low levels of Ag doping can suppress disorder only under Cu-rich and constrained Cu-poor conditions. Additionally, we expect Cd_{Zn} and Ag_{Cu} isovalent dopants to form deep acceptor trap states, while Ag_{Zn} should lead to a large increase in free hole concentration under Cu-poor conditions. Note that low levels of Ag doping under Cu-rich conditions will reduce the concentration of Cu vacancies, which are responsible for the p-type behavior of Cu_2ZnSnS_4 and flattening the band edge fluctuations.[23] On the other hand, high levels of Cd (Ag) doping can be detrimental (beneficial) because of the stabilization (destabilization) of the lower-band-gap stannite structure. Also, we find that the constrained Cu-poor conditions, which correspond to the lowest Cu content used during the synthesis of Cu_2ZnSnS_4 under the constraint of high Zn and high Sn contents, are beneficial in reducing disorder at low levels of Cd and Ag doping, in qualitative agreement with previous theoretical and experimental studies. We attribute any grain growth observed during synthesis to the high temperatures employed during selenization, given that our calculations indicate a negligible influence of Cd doping on surface energies while Ag doping causes a significant decrease that would favor smaller, not larger, grains. Finally, as an immediate extension of this study, we suggest the exploration of alternate abundant, nontoxic, and isovalent dopants to further improve the efficiencies of Cu_2ZnSnS_4-based solar cells.

ASSOCIATED CONTENT

Supporting Information

The Supporting Information is available free of charge on the ACS Publications website at DOI: 10.1021/acs.chemmater.8b00677.

Benchmarks of binary sulfide formation energies and lattice parameters of Cu_2ZnSnS_4 and SnS_2; total densities of states of kesterite and stannite using various DFT-based approximations; description of all compounds, structures, and constraints used in estimating reported elemental chemical potentials; and schematics of electrostatic correction schemes employed, convergence of charged defect formation energies, and final electrostatic corrections calculated for all charged defects considered (PDF)

AUTHOR INFORMATION

Corresponding Author

*E-mail: eac@princeton.edu.

ORCID

Gopalakrishnan Sai Gautam: 0000-0002-1303-0976
Thomas P. Senftle: 0000-0002-5889-5009
Emily A. Carter: 0000-0001-7330-7554

Present Address

§T.P.S.: Department of Chemical and Biomolecular Engineering, Rice University, Houston, TX 77005.

Notes

The authors declare no competing financial interest.

ACKNOWLEDGMENTS

E.A.C. thanks the U.S. Department of Energy, Office of Science, Basic Energy Sciences, under Grant DE-SC0002120 for funding this project. The authors thank Dr. Johannes M. Dieterich and Ms. Nari L. Baughman for a careful reading of the manuscript.

REFERENCES

(1) National Renewable Energy Laboratory. Research cell efficiency records chart. https://www.nrel.gov/pv/assets/images/efficiency-chart.png.

(2) Green, M. A.; Emery, K.; Hishikawa, Y.; Warta, W.; Dunlop, E. D. Solar Cell Efficiency Tables (Version 45). *Prog. Photovoltaics* **2015**, *23*, 1−9.

(3) Branker, K.; Pathak, M. J. M.; Pearce, J. M. A Review of Solar Photovoltaic Levelized Cost of Electricity. *Renewable Sustainable Energy Rev.* **2011**, *15*, 4470−4482.

(4) Bernardi, M.; Palummo, M.; Grossman, J. C. Extraordinary Sunlight Absorption and One Nanometer Thick Photovoltaics Using Two-Dimensional Monolayer Materials. *Nano Lett.* **2013**, *13*, 3664−3670.

(5) Nakayama, K.; Tanabe, K.; Atwater, H. A. Plasmonic Nanoparticle Enhanced Light Absorption in GaAs Solar Cells. *Appl. Phys. Lett.* **2008**, *93*, 121904.

(6) Gloeckler, M.; Sankin, I.; Zhao, Z. CdTe Solar Cells at the Threshold to 20% Efficiency. *IEEE J. Photovoltaics* **2013**, *3*, 1389−1393.

(7) Jackson, P.; Hariskos, D.; Wuerz, R.; Kiowski, O.; Bauer, A.; Friedlmeier, T. M.; Powalla, M. Properties of Cu(In,Ga)Se2 Solar Cells with New Record Efficiencies up to 21.7%. *Phys. Status Solidi RRL* **2015**, *9*, 28−31.

(8) Yang, W. S.; Noh, J. H.; Jeon, N. J.; Kim, Y. C.; Ryu, S.; Seo, J.; Seok, S. I. High-Performance Photovoltaic Perovskite Layers Fabricated through Intramolecular Exchange. *Science (Washington, DC, U. S.)* **2015**, *348*, 1234−1237.

(9) Andersson, B. A. Materials Availability for Large-Scale Thin-Film Photovoltaics. *Prog. Photovoltaics* **2000**, *8*, 61−76.

(10) Delbos, S. Kesterite Thin Films for Photovoltaics : A Review. *EPJ Photovoltaics* **2012**, *3*, 35004.

(11) Walsh, A.; Chen, S.; Wei, S.-H.; Gong, X.-G. Kesterite Thin-Film Solar Cells: Advances in Materials Modelling of Cu2ZnSnS4. *Adv. Energy Mater.* **2012**, *2*, 400−409.

(12) Ford, G. M.; Guo, Q.; Agrawal, R.; Hillhouse, H. W. Earth Abundant Element Cu2Zn(Sn1− xGex)S4 Nanocrystals for Tunable Band Gap Solar Cells: 6.8% Efficient Device Fabrication. *Chem. Mater.* **2011**, *23*, 2626−2629.

(13) Siebentritt, S.; Schorr, S. Kesterites-a Challenging Material for Solar Cells. *Prog. Photovoltaics* **2012**, *20*, 512−519.

(14) Barkhouse, D. A. R.; Gunawan, O.; Gokmen, T.; Todorov, T. K.; Mitzi, D. B. Device Characteristics of a 10.1% Hydrazine-Processed Cu2ZnSn(Se,S)4 Solar Cell. *Prog. Photovoltaics* **2012**, *20*, 6−11.

(15) Wang, W.; Winkler, M. T.; Gunawan, O.; Gokmen, T.; Todorov, T. K.; Zhu, Y.; Mitzi, D. B. Device Characteristics of CZTSSe Thin-Film Solar Cells with 12.6% Efficiency. *Adv. Energy Mater.* **2014**, *4*, 1301465.

DOI: 10.1021/acs.chemmater.8b00677
Chem. Mater. 2018, 30, 4543−4555

(16) Bosson, C. J.; Birch, M. T.; Halliday, D. P.; Tang, C. C.; Kleppe, A. K.; Hatton, P. D. Polymorphism in Cu2ZnSnS 4 and New Off-Stoichiometric Crystal Structure Types. *Chem. Mater.* **2017**, *29*, 9829−9839.
(17) Paris, M.; Choubrac, L.; Lafond, A.; Guillot-Deudon, C.; Jobic, S. Solid-State NMR and Raman Spectroscopy To Address the Local Structure of Defects and the Tricky Issue of the Cu/Zn Disorder in Cu-Poor, Zn-Rich CZTS Materials. *Inorg. Chem.* **2014**, *53*, 8646−8653.
(18) Scragg, J. J. S.; Choubrac, L.; Lafond, A.; Ericson, T.; Platzer-Björkman, C. A Low-Temperature Order-Disorder Transition in Cu2ZnSnS4 Thin Films. *Appl. Phys. Lett.* **2014**, *104*, 041911.
(19) Rey, G.; Redinger, A.; Sendler, J.; Weiss, T. P.; Thevenin, M.; Guennou, M.; El Adib, B.; Siebentritt, S. The Band Gap of Cu2ZnSnSe4: Effect of Order-Disorder. *Appl. Phys. Lett.* **2014**, *105*, 112106.
(20) Chen, S.; Walsh, A.; Gong, X.-G.; Wei, S.-H. Classification of Lattice Defects in the Kesterite Cu2ZnSnS4 and Cu2ZnSnSe4 Earth-Abundant Solar Cell Absorbers. *Adv. Mater.* **2013**, *25*, 1522−1539.
(21) Yu, K.; Carter, E. A. A Strategy to Stabilize Kesterite CZTS for High-Performance Solar Cells. *Chem. Mater.* **2015**, *27*, 2920−2927.
(22) Chen, S.; Yang, J.-H.; Gong, X. G.; Walsh, A.; Wei, S.-H. Intrinsic Point Defects and Complexes in the Quaternary Kesterite Semiconductor Cu2ZnSnS4. *Phys. Rev. B: Condens. Matter Mater. Phys.* **2010**, *81*, 245204.
(23) Yu, K.; Carter, E. A. Elucidating Structural Disorder and the Effects of Cu Vacancies on the Electronic Properties of Cu2ZnSnS4. *Chem. Mater.* **2016**, *28*, 864−869.
(24) Yu, K.; Carter, E. A. Determining and Controlling the Stoichiometry of Cu2ZnSnS 4 Photovoltaics: The Physics and Its Implications. *Chem. Mater.* **2016**, *28*, 4415−4420.
(25) Redinger, A.; Berg, D. M.; Dale, P. J.; Djemour, R.; Gütay, L.; Eisenbarth, T.; Valle, N.; Siebentritt, S. Route Toward High-Efficiency Single-Phase Cu2ZnSn(S,Se)4 Thin-Film Solar Cells: Model Experiments and Literature Review. *IEEE J. Photovoltaics* **2011**, *1*, 200−206.
(26) Redinger, A.; Berg, D. M.; Dale, P. J.; Siebentritt, S. The Consequences of Kesterite Equilibria for Efficient Solar Cells. *J. Am. Chem. Soc.* **2011**, *133*, 3320−3323.
(27) Maeda, T.; Nakamura, S.; Wada, T. First-Principles Study on Cd Doping in Cu2ZnSnS4 and Cu2ZnSnSe4. *Jpn. J. Appl. Phys.* **2012**, *51*, 10NC11.
(28) Yuan, Z.-K.; Chen, S.; Xiang, H.; Gong, X.-G.; Walsh, A.; Park, J.-S.; Repins, I.; Wei, S.-H. Engineering Solar Cell Absorbers by Exploring the Band Alignment and Defect Disparity: The Case of Cu- and Ag-Based Kesterite Compounds. *Adv. Funct. Mater.* **2015**, *25*, 6733−6743.
(29) Shannon, R. D.; Prewitt, C. T. Effective Ionic Radii in Oxides and Fluorides. *Acta Crystallogr., Sect. B: Struct. Crystallogr. Cryst. Chem.* **1969**, *25*, 925−946.
(30) Fu, J.; Tian, Q.; Zhou, Z.; Kou, D.; Meng, Y.; Zhou, W.; Wu, S. Improving the Performance of Solution-Processed Cu2ZnSn(S,Se)4 Photovoltaic Materials by Cd2+ Substitution. *Chem. Mater.* **2016**, *28*, 5821−5828.
(31) Qi, Y.; Tian, Q.; Meng, Y.; Kou, D.; Zhou, Z.; Zhou, W.; Wu, S. Elemental Precursor Solution Processed (Cu1− xAgx)2ZnSn(S,Se)4 Photovoltaic Devices with over 10% Efficiency. *ACS Appl. Mater. Interfaces* **2017**, *9*, 21243−21250.
(32) Qi, Y.-F.; Kou, D.-X.; Zhou, W.-H.; Zhou, Z.-J.; Tian, Q.-W.; Meng, Y.-N.; Liu, X.-S.; Du, Z.-L.; Wu, S.-X. Engineering of Interface Band Bending and Defects Elimination via a Ag-Graded Active Layer for Efficient (Cu,Ag)2ZnSn(S,Se)4 Solar Cells. *Energy Environ. Sci.* **2017**, *10*, 2401−2410.
(33) Guchhait, A.; Su, Z.; Tay, Y. F.; Shukla, S.; Li, W.; Leow, S. W.; Tan, J. M. R.; Lie, S.; Gunawan, O.; Wong, L. H. Enhancement of Open-Circuit Voltage of Solution-Processed Cu2ZnSnS4 Solar Cells with 7.2% Efficiency by Incorporation of Silver. *ACS Energy Lett.* **2016**, *1*, 1256−1261.
(34) Yan, C.; Sun, K.; Huang, J.; Johnston, S.; Liu, F.; Veettil, B. P.; Sun, K.; Pu, A.; Zhou, F.; Stride, J. A.; et al. Beyond 11% Efficient Sulfide Kesterite Cu 2 Zn X Cd 1− X SnS 4 Solar Cell: Effects of Cadmium Alloying. *ACS Energy Lett.* **2017**, *2*, 930−936.
(35) Hohenberg, P.; Kohn, W. Inhomogeneous Electron Gas. *Phys. Rev.* **1964**, *136*, B864−B871.
(36) Kohn, W.; Sham, L. J. Self-Consistent Equations Including Exchange and Correlation Effects. *Phys. Rev.* **1965**, *140*, A1133−A1138.
(37) Jackson, A. J.; Walsh, A. Ab Initio Thermodynamic Model of Cu2ZnSnS4. *J. Mater. Chem. A* **2014**, *2*, 7829−7836.
(38) Xu, P.; Chen, S.; Huang, B.; Xiang, H. J.; Gong, X.-G.; Wei, S.-H. Stability and Electronic Structure of Cu2ZnSnS4 Surfaces: First-Principles Study. *Phys. Rev. B: Condens. Matter Mater. Phys.* **2013**, *88*, 45427.
(39) Kumar, S.; Sharma, D. K.; Auluck, S. Stability, Electronic, and Optical Properties of Wurtzite Cu2CdxZn1−xSnS4. *Phys. Rev. B: Condens. Matter Mater. Phys.* **2016**, *94*, 235206.
(40) Kresse, G.; Hafner, J. Ab Initio Molecular Dynamics for Liquid Metals. *Phys. Rev. B: Condens. Matter Mater. Phys.* **1993**, *47*, 558−561.
(41) Kresse, G.; Furthmüller, J. Efficient Iterative Schemes for Ab Initio Total-Energy Calculations Using a Plane-Wave Basis Set. *Phys. Rev. B: Condens. Matter Mater. Phys.* **1996**, *54*, 11169−11186.
(42) Kresse, G.; Joubert, D. From Ultrasoft Pseudopotentials to the Projector Augmented-Wave Method. *Phys. Rev. B: Condens. Matter Mater. Phys.* **1999**, *59*, 1758−1775.
(43) Calderon, C. E.; Plata, J. J.; Toher, C.; Oses, C.; Levy, O.; Fornari, M.; Natan, A.; Mehl, M. J.; Hart, G.; Buongiorno Nardelli, M.; et al. The AFLOW Standard for High-Throughput Materials Science Calculations. *Comput. Mater. Sci.* **2015**, *108*, 233−238.
(44) Sun, J.; Ruzsinszky, A.; Perdew, J. P. Strongly Constrained and Appropriately Normed Semilocal Density Functional. *Phys. Rev. Lett.* **2015**, *115*, 36402.
(45) Car, R. Density Functional Theory: Fixing Jacob's Ladder. *Nat. Chem.* **2016**, *8*, 820−821.
(46) Perdew, J. P.; Burke, K.; Ernzerhof, M. Generalized Gradient Approximation Made Simple. *Phys. Rev. Lett.* **1996**, *77*, 3865−3868.
(47) Katagiri, H.; Saitoh, K.; Washio, T.; Shinohara, H.; Kurumadani, T.; Miyajima, S. Development of Thin Film Solar Cell Based on Cu2ZnSnS4 Thin Films. *Sol. Energy Mater. Sol. Cells* **2001**, *65*, 141−148.
(48) Tanaka, T.; Nagatomo, T.; Kawasaki, D.; Nishio, M.; Guo, Q.; Wakahara, A.; Yoshida, A.; Ogawa, H. Preparation of Cu2ZnSnS4 Thin Films by Hybrid Sputtering. *J. Phys. Chem. Solids* **2005**, *66*, 1978−1981.
(49) Botti, S.; Kammerlander, D.; Marques, M. A. L. Band Structures of Cu2ZnSnS4 and Cu2ZnSnSe4 from Many-Body Methods. *Appl. Phys. Lett.* **2011**, *98*, 241915.
(50) Freysoldt, C.; Grabowski, B.; Hickel, T.; Neugebauer, J.; Kresse, G.; Janotti, A.; Van de Walle, C. G. First-Principles Calculations for Point Defects in Solids. *Rev. Mod. Phys.* **2014**, *86*, 253−305.
(51) Anisimov, V. I.; Zaanen, J.; Andersen, O. K. Band Theory and Mott Insulators: Hubbard U instead of Stoner I. *Phys. Rev. B: Condens. Matter Mater. Phys.* **1991**, *44*, 943−954.
(52) Grimme, S. Semiempirical GGA-Type Density Functional Constructed with a Long-Range Dispersion Correction. *J. Comput. Chem.* **2006**, *27*, 1787−1799.
(53) Yu, K.; Carter, E. A. Communication: Comparing Ab Initio Methods of Obtaining Effective U Parameters for Closed-Shell Materials. *J. Chem. Phys.* **2014**, *140*, 121105.
(54) Inorganic Crystal Structure Database (ICSD). https://www.fiz-karlsruhe.de/en/leistungen/kristallographie/icsd.html.
(55) Watson, G. W.; Kelsey, E. T.; de Leeuw, N. H.; Harris, D. J.; Parker, S. C. Atomistic Simulation of Dislocations, Surfaces and Interfaces in MgO. *J. Chem. Soc., Faraday Trans.* **1996**, *92*, 433.
(56) Ramamoorthy, M.; Vanderbilt, D.; King-Smith, R. D. First-Principles Calculations of the Energetics of Stoichiometric TiO2

DOI: 10.1021/acs.chemmater.8b00677
Chem. Mater. 2018, 30, 4543−4555

Surfaces. *Phys. Rev. B: Condens. Matter Mater. Phys.* **1994**, *49*, 16721−16727.
(57) Wang, L.; Zhou, F.; Meng, Y. S.; Ceder, G. First-Principles Study of Surface Properties of LiFePO4 : Surface Energy, Wulff Shape, and Surface Redox Potential. *Phys. Rev. B: Condens. Matter Mater. Phys.* **2007**, *76*, 165435.
(58) Kramer, D.; Ceder, G. Tailoring the Morphology of LiCoO2 : A First Principles Study. *Chem. Mater.* **2009**, *21*, 3799−3809.
(59) Moll, N.; Kley, A.; Pehlke, E.; Scheffler, M. GaAs Equilibrium Crystal Shape from First Principles. *Phys. Rev. B: Condens. Matter Mater. Phys.* **1996**, *54*, 8844−8855.
(60) Shiraishi, K. A New Slab Model Approach for Electronic Structure Calculation of Polar Semiconductor Surface. *J. Phys. Soc. Jpn.* **1990**, *59*, 3455−3458.
(61) Harrison, W. A. Theory of Polar Semiconductor Surfaces. *J. Vac. Sci. Technol.* **1979**, *16*, 1492−1496.
(62) Pashley, M. D. Electron Counting Model and Its Application to Island Structures on Molecular-Beam Epitaxy Grown GaAs(001) and ZnSe(001). *Phys. Rev. B: Condens. Matter Mater. Phys.* **1989**, *40*, 10481−10487.
(63) Zhang, S. B.; Wei, S.-H. Surface Energy and the Common Dangling Bond Rule for Semiconductors. *Phys. Rev. Lett.* **2004**, *92*, 86102.
(64) Freysoldt, C.; Neugebauer, J.; Van de Walle, C. G. Fully Ab Initio Finite-Size Corrections for Charged-Defect Supercell Calculations. *Phys. Rev. Lett.* **2009**, *102*, 16402.
(65) Kumagai, Y.; Oba, F. Electrostatics-Based Finite-Size Corrections for First-Principles Point Defect Calculations. *Phys. Rev. B: Condens. Matter Mater. Phys.* **2014**, *89*, 195205.
(66) Freysoldt, C.; Neugebauer, J.; Van de Walle, C. G. Electrostatic Interactions between Charged Defects in Supercells. Phys. *Phys. Status Solidi B* **2011**, *248*, 1067−1076.
(67) Broberg, D.; Medasani, B.; Zimmermann, N. E. R.; Yu, G.; Canning, A.; Haranczyk, M.; Asta, M.; Hautier, G. PyCDT: A Python Toolkit for Modeling Point Defects in Semiconductors and Insulators. *Comput. Phys. Commun.* **2018**, *226*, 165−179.
(68) Ong, S. P.; Richards, W. D.; Jain, A.; Hautier, G.; Kocher, M.; Cholia, S.; Gunter, D.; Chevrier, V. L.; Persson, K. a.; Ceder, G. Python Materials Genomics (Pymatgen): A Robust, Open-Source Python Library for Materials Analysis. *Comput. Mater. Sci.* **2013**, *68*, 314−319.
(69) Canepa, P.; Sai Gautam, G.; Broberg, D.; Bo, S.-H.; Ceder, G. Role of Point Defects in Spinel Mg Chalcogenide Conductors. *Chem. Mater.* **2017**, *29*, 9657−9667.
(70) Weil, J. A. A. Review of Electron Spin Spectroscopy and Its Application to the Study of Paramagnetic Defects in Crystalline Quartz. *Phys. Chem. Miner.* **1984**, *10*, 149−165.
(71) Hume-Rothery, W.; Powell, H. M. On the Theory of Super-Lattice Structures in Alloys. *Z. Kristallogr. - Cryst. Mater.* **1935**, *91*, 23−47.
(72) Perdew, J. P. Density Functional Theory and the Band Gap Problem. *Int. J. Quantum Chem.* **1985**, *28*, 497−523.
(73) Hybertsen, M. S.; Louie, S. G. First-Principles Theory of Quasiparticles: Calculation of Band Gaps in Semiconductors and Insulators. *Phys. Rev. Lett.* **1985**, *55*, 1418−1421.
(74) Matsushita, H.; Ichikawa, T.; Katsui, A. Structural, Thermodynamical and Optical Properties of Cu2-II-IV-VI4 Quaternary Compounds. *J. Mater. Sci.* **2005**, *40*, 2003−2005.
(75) Gong, W.; Tabata, T.; Takei, K.; Morihama, M.; Maeda, T.; Wada, T. Crystallographic and Optical Properties of (Cu,Ag)-2ZnSnS4 and (Cu,Ag)2ZnSnSe4 Solid Solutions. Phys. *Status Solidi C* **2015**, *12*, 700−703.
(76) Tasker, P. W. The Stability of Ionic Crystal Surfaces. *J. Phys. C: Solid State Phys.* **1979**, *12*, 4977−4984.
(77) Wang, G.; Zhao, W.; Cui, Y.; Tian, Q.; Gao, S.; Huang, L.; Pan, D. Fabrication of a $Cu_2ZnSn(S,Se)_4$ Photovoltaic Device by a Low-Toxicity Ethanol Solution Process. *ACS Appl. Mater. Interfaces* **2013**, *5*, 10042−10047.
(78) Ewald, P. P. Die Berechnung Optischer Und Elektrostatischer Gitterpotentiale. *Ann. Phys.* **1921**, *369*, 253−287.
(79) Nagaoka, A.; Miyake, H.; Taniyama, T.; Kakimoto, K.; Nose, Y.; Scarpulla, M. A.; Yoshino, K. Effects of Sodium on Electrical Properties in Cu2ZnSnS4 Single Crystal. *Appl. Phys. Lett.* **2014**, *104*, 152101.
(80) Kuo, D.-H.; Wubet, W. Mg Dopant in Cu2ZnSnSe4: An N-Type Former and a Promoter of Electrical Mobility up to 120cm2V−1s−1. *J. Solid State Chem.* **2014**, *215*, 122−127.
(81) Tablero, C. Electronic and Photon Absorber Properties of Cr-Doped Cu2ZnSnS4. *J. Phys. Chem. C* **2012**, *116*, 23224−23230.

DOI: 10.1021/acs.chemmater.8b00677
Chem. Mater. 2018, 30, 4543−4555